



A Framework to Calibrate a Semianalytic Model of the First Stars and Galaxies to the Renaissance Simulations

Ryan Hazlett¹ , Mihir Kulkarni¹ , Eli Visbal¹ , and John H. Wise²

¹ Ritter Astrophysical Research Center, Department of Physics and Astronomy, University of Toledo, 2801 West Bancroft Street, Toledo, OH 43606, USA;
ryan.hazlett@rockets.utoledo.edu, mihir.kulkarni@utoledo.edu, elijah.visbal@utoledo.edu

² Center for Relativistic Astrophysics, Georgia Institute of Technology, 837 State Street, Atlanta, GA 30332, USA; jwise@physics.gatech.edu

Received 2024 March 8; revised 2024 November 5; accepted 2024 November 10; published 2024 December 20

Abstract

We present a method that calibrates a semianalytic model to the Renaissance Simulations, a suite of cosmological hydrodynamical simulations with high-redshift galaxy formation. This approach combines the strengths of semianalytic techniques and hydrodynamical simulations, enabling the extension to larger volumes and lower redshifts that are inaccessible to simulations due to computational expense. Using a sample of Renaissance star formation histories from an average density region of the Universe, we construct a four-parameter prescription for metal-enriched star formation characterized by an initial bursty stage followed by a steady stage where stars are formed at constant efficiencies. Our model also includes a treatment of Pop III star formation where a minimum halo mass and log-normal distribution of stellar mass are adopted to match the numerical simulations. Star formation is generally well reproduced for halos with masses $\lesssim 10^9 M_\odot$. Between $11 < z < 25$ our model produces metal-enriched star formation rate densities (SFRDs) that typically agree with Renaissance within a factor of ~ 2 for the average density region. Additionally, the total metal-enriched stellar mass only differs from Renaissance by about 10% at $z \sim 11$. For regions that are either more overdense or rarefied and not included in the calibration, we produce metal-enriched SFRDs that agree with Renaissance within a factor of ~ 2 at high- z but eventually differ by higher factors for later times. This is likely due to environmental dependencies not included in the model. Our star formation prescriptions can easily be adopted in other analytic or semianalytic works to match our calibration to Renaissance.

Unified Astronomy Thesaurus concepts: Population III stars (1285); Galaxy formation (595); High-redshift galaxies (734); Cosmology (343)

1. Introduction

Understanding the first stars and galaxies is one of the major goals of modern astronomy. In the context of the Λ Cold Dark Matter (Λ CDM) model of cosmology, simulations, and analytic calculations predict that the first Population III (Pop III) stars formed from primordial gas within $\sim 10^8$ yr after the Big Bang via molecular hydrogen cooling in $\sim 10^{5-6} M_\odot$ dark matter (DM) “minihalos” (Z. Haiman et al. 1996b; M. Tegmark et al. 1997; T. Abel et al. 2002; N. Yoshida et al. 2003; B. W. O’Shea & M. L. Norman 2007; J. H. Wise & T. Abel 2007; T. H. Greif 2015; M. Kulkarni et al. 2021; A. T. P. Schauer et al. 2021; S. Hegde & S. R. Furlanetto 2023; O. Nebrin et al. 2023). Due to less efficient gas cooling during star formation, Pop III stars are expected to have higher masses than Population II/I, perhaps with typical values of $\sim 10\text{--}1000 M_\odot$ (T. H. Greif et al. 2011; T. Hosokawa et al. 2011; S. Hirano et al. 2014; H. Susa et al. 2014; M. N. Ishigaki et al. 2018), but the precise initial mass function (IMF) remains uncertain.

We note that because the very first stars are predicted to form in small numbers at very high redshifts ($z \gtrsim 20$), they are unlikely to be directly observed, even with the James Webb Space Telescope (JWST). However, most models predict that Pop III star formation should continue well into or beyond the epoch of reionization (S. Riaz et al. 2022; J. Borrow et al. 2023) where they might be detected either as purely Pop III galaxies or in mixtures of Pop III and metal-enriched star

formation (e.g., in the case of inefficient metal-mixing). In fact, there are already some exciting but tentative or unconfirmed Pop III signatures from JWST (R. Maiolino et al. 2024; X. Wang et al. 2024). Other promising observational probes of Pop III stars include He II line intensity mapping (E. Visbal et al. 2015; J. Parsons et al. 2022), pair-instability supernovae (PISNe) detection (D. J. Whalen et al. 2013a; T. Hartwig et al. 2018), 21 cm cosmology (E. Visbal et al. 2012; A. Fialkov et al. 2013; A. Cohen et al. 2017; J. D. Bowman et al. 2018), and stellar archeology (A. Frebel & J. E. Norris 2015).

Due to the hierarchical character of large-scale structure formation in Λ CDM, the minihalos hosting Pop III stars serve as building blocks for the first metal-enriched galaxies. Thus, the properties of high-redshift low-mass galaxies observable with JWST are expected to depend on the details of Pop III star formation. For example, M. Abe et al. (2021) found that a top-heavy Pop III IMF, which results in more highly energetic PISNe, results in suppressed star formation in galaxies hosted by $\sim 10^9 M_\odot$ halos. Understanding the first metal-enriched galaxies is also interesting because they may drive the process of cosmic reionization, they represent the earliest stages of more evolved galaxies, and the existence of low-mass DM host halos puts constraints on alternative DM models, such as “fuzzy” or warm DM (L. Gao & T. Theuns 2007; P. Mocz et al. 2019, 2020; M. Kulkarni et al. 2022), that suppress small-scale structure. Using JWST, we are able to study these galaxies individually and determine their global properties through quantities such as the UV luminosity function (R. J. Bouwens et al. 2023; H. Atek et al. 2024).

Theoretical models are required to interpret and guide the observations of the first stars and galaxies described above.



Original content from this work may be used under the terms of the [Creative Commons Attribution 4.0 licence](#). Any further distribution of this work must maintain attribution to the author(s) and the title of the work, journal citation and DOI.

Hydrodynamical cosmological simulations are a primary tool that has been used. State-of-the-art simulations can include a variety of physical processes, such as gas chemistry/cooling, radiative transfer of UV photons, and feedback from supernovae (SNe) explosion. These effects can be modeled with high fidelity, but have the drawback of being numerically expensive. For instance, the Renaissance Simulations, described in detail below, used around 10 million CPU hours on the NCSA Blue Waters supercomputers to run a box size of 135 Mpc^3 to a redshift of $z \sim 15$ (P. Chen et al. 2014; H. Xu et al. 2014).

This presents a serious challenge because in order to make predictions for the observations described above one needs much larger volumes than can be modeled with hydrodynamical simulations. For example, in order to understand the impact of Pop III stars on low-mass galaxies, one needs a large-statistical sample of galaxies forming in $\sim 10^9 M_\odot$ DM halos, but would also need to resolve the low-mass halos that host Pop III star formation. Despite its computational expense, the Renaissance volume that can be simulated only contains a few thousand of these objects, much less than required for robust statistical analysis.

A different technique is to use computationally efficient semianalytic models that combine analytic prescriptions with DM halo merger trees generated from N -body simulations or Monte Carlo methods. Semianalytic simulations have been used extensively to study the first stars and galaxies (e.g., M. Trenti & M. Stiavelli 2009; B. D. Crosby et al. 2013; R. H. Mebane et al. 2018; E. Visbal et al. 2018; L. Y. A. Yung et al. 2019; B. Liu & V. Bromm 2020). These simulations are able to rapidly scan the relevant parameter space (e.g., the Pop III IMF and critical metallicity for Pop III star formation). However, the main drawback of this type of modeling is that a large number of free parameters are often employed and it can be unclear to what extent analytic assumptions are justified.

In this paper, we explore using the Renaissance simulations to perform a detailed calibration of a semianalytic model of the first stars (E. Visbal et al. 2020). The goal of this exercise is to obtain a model that is both computationally efficient and well matched to detailed numerical simulations. This enables the simulation results to be extended to much larger volumes such that observational predictions become possible. To achieve this goal, we develop an empirically calibrated star formation model based on the Renaissance results. We include both Pop III and metal-enriched star formation, but the emphasis is on metal-enriched because the halos hosting early Pop III star formation are not well resolved. Our empirical calibration includes a number of parameters, such as metal-enriched starburst mass, quiescent period following a burst, etc., that are measured directly from the simulations. This model and parameterization can easily be applied to other semianalytic models or analytic calculations in the future.

This study is related to that of J. McCaffrey et al. (2023), which calibrates a semianalytic model to Renaissance. We note that in this case, only the largest galaxy in Renaissance was considered and the simulation data sets used were unable to resolve the formation of Pop III. As explained in detail below, we find that while our prescription is calibrated to a region at the mean density of the Universe, it can reproduce the star formation rate density (SFRD) typically within a factor of ~ 2 without any calibration on such a region. Thus, we have shown that a calibration framework such as that developed in this

paper can extend the reach of numerical simulations, both in volume and range of cosmic time.

This paper is structured as follows. In Section 2, we review the main features of the Renaissance simulation suite. In Section 3, we describe our parameterization of metal-enriched and Pop III star formation in Renaissance along with our sample. In Section 4, we present the calibration of a semianalytic model to Renaissance along with our results for metal-enriched and Pop III star formation. Finally, we summarize the results and discuss our main conclusions in Section 5. Throughout, we assume a cosmology consistent with Renaissance using parameters from the WMAP7 Λ CDM+SZ+LENS best fit (E. Komatsu et al. 2011) with $\Omega_M = 0.266$, $\Omega_\Lambda = 0.734$, $\Omega_b = 0.0449$, $h = 0.71$, $\sigma_8 = 0.81$, and $n = 0.963$.

2. The Renaissance Simulations

The Renaissance Simulations are cosmological hydrodynamics simulations that were performed with the adaptive mesh refinement code ENZO (G. L. Bryan et al. 2014; C. Brummel-Smith et al. 2019) to simulate the formation of the first stars and galaxies. Radiative transfer from ionizing radiation is calculated with the MORAY package (J. H. Wise & T. Abel 2011) along with chemistry and cooling for nine species of hydrogen and helium (T. Abel et al. 1997) and metallicity dependent cooling tables (B. D. Smith et al. 2009).

Renaissance consists of three different regions taken from a comoving volume of $(40 \text{ Mpc})^3$. The three regions, named “RarePeak,” “Normal,” and “Void,” are in overdense, average, or underdense regions and evolved to redshifts of $z = 15, 12.5$, and 8 . RarePeak has a comoving volume of $(3.8 \times 5.4 \times 6.6) \text{ Mpc}^3$, and Normal and Void have comoving volumes of $(6.0 \times 6.0 \times 6.125) \text{ Mpc}^3$, respectively (B. W. O’Shea et al. 2015). Our semianalytic model calibration is focused on the Normal region, and then applied to RarePeak and Void for comparison.

It is important to emphasize key aspects of the metal-enriched and Pop III star formation prescriptions in Renaissance due to their importance in our star formation calibration. The metal-enriched star clusters are formed from molecular clouds with a typical radius of $\sim 6 \text{ pc}$. The clusters have a total stellar mass populated with stars assuming a Salpeter IMF and emit 6000 hydrogen ionizing photons per stellar baryon over 20 Myr (the maximum lifetime of an OB star). After 4 Myr, the clusters generate $6.8 \times 10^{48} \text{ erg } M_\odot^{-1}$ for SNe feedback. For Pop III, individual stars are formed before the metal-enriched star clusters with a mass randomly sampled from a power-law IMF similar to a Salpeter IMF with an exponential decrease below a characteristic mass of $M_{\text{char}} = 40 M_\odot$. Stellar lifetimes along with Lyman–Werner (LW) and hydrogen ionizing photon luminosities are drawn from D. Schaerer (2002). Stars in the mass ranges of $11\text{--}20 M_\odot$, $20\text{--}40 M_\odot$, and $140\text{--}260 M_\odot$ explode as Type II SNe and hypernovae (K. Nomoto et al. 2006), and PISNe (A. Heger et al. 2003), respectively with energies exceeding 10^{51} erg . Stars with masses outside these ranges directly collapse into a black hole without an explosion. Further details can be found in J. H. Wise et al. (2012a).

High-redshift galaxy observations from the CEERS (S. L. Finkelstein et al. 2023) and JADES surveys (D. J. Eisenstein et al. 2023) imply that star formation rates are likely higher than predicted by previous simulations (P. Arrabal Haro et al. 2023; A. J. Bunker et al. 2023). J. McCaffrey et al. (2023) recently demonstrated that early Renaissance galaxies typically

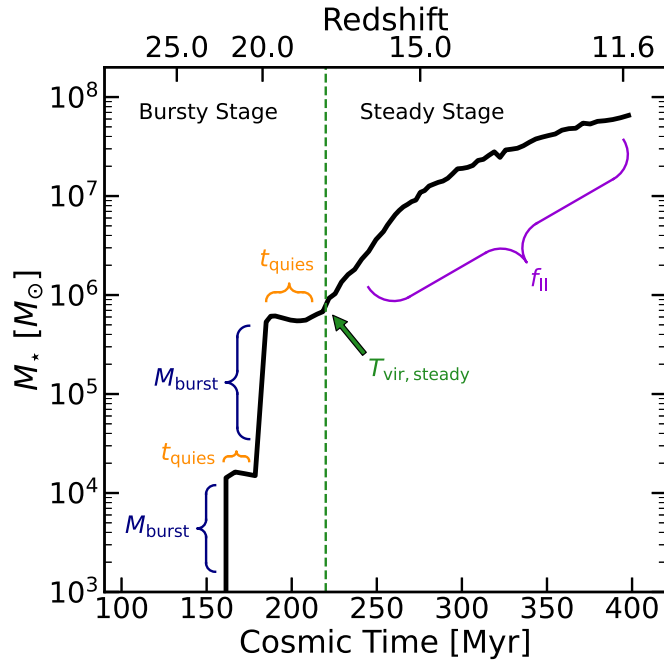


Figure 1. Metal-enriched SFHs for a single Renaissance halo. M_* is the total mass of metal-enriched stars formed in the halo. This halo experiences two episodes of bursty star formation followed by a stage of steady star formation once the halo reaches a virial temperature threshold. The burst stellar mass, quiescent period, ionization feedback threshold temperature, and steady star formation efficiency are labeled M_{burst} , t_{quies} , $T_{\text{vir, steady}}$, and f_{II} , respectively. Bursty and steady stages are found throughout the sample of halos we analyze.

experience rapid star formation, with a specific star formation rate of $\sim 10^{-8} \text{ yr}^{-1}$, which is consistent with the galaxies observed by CEERS and JADES. This agreement suggests that Renaissance is a good choice for calibration to high- z galaxy formation.

3. Calibration to Renaissance

3.1. Overview

We examined star formation histories (SFHs) for a wide selection of Renaissance halos, building up a representative sample detailed in Section 3.2. In Figure 1, we show the metal-enriched SFH for the most massive halo in the Normal region. Stellar evolution in this halo is representative of trends typically found in other Renaissance halos. We find after the first generation of stars, star formation proceeds through two distinct stages—a bursty stage characterized by rapid star formation followed by a steady stage with stars forming at a more constant rate. The division of metal-enriched star formation into bursty and steady stages is the foundation for our calibration to Renaissance and later implementation in our semianalytic model.

The bursty stage begins with the first instance of metal-enriched star formation following the death of Pop III stars and dispersal of their metals into the interstellar medium (ISM). We do not include external enrichment in this analysis, as discussed further in Section 4. Forming in low-mass halos at high redshift, metal-enriched stars form in a rapid starburst at the onset of the bursty stage. SNe feedback from stars formed in the burst disperses any dense clumps and expels most of the gas from the shallow gravitational potential well. Following the expulsion of gas, star formation enters an extended quiescent period as gas falls back into the halo and dense clumps begin to

reform. A halo can experience multiple bursts and quiescent periods dependent on its virial mass, see Section 3.3.1 for more detail.

After the initial bursty stage, a change in star formation occurs as the steady stage begins. This transition corresponds to a fixed virial temperature that is consistent with the halo mass below which reionization has been shown to suppress star formation as a result of gas photoheating (e.g., P. R. Shapiro et al. 1994; A. A. Thoul & D. H. Weinberg 1996; N. Y. Gnedin & L. Hui 1998; N. Y. Gnedin 2000; M. Dijkstra et al. 2004; M. Hoeft et al. 2006; T. Okamoto et al. 2008; E. Sobacchi & A. Mesinger 2013; Y. Noh & M. McQuinn 2014). Once the steady stage begins, the halo is sufficiently massive to retain enough gas to fuel continuous future star formation. Total metal-enriched star formation produced during the steady stage eventually completely dominates at lower redshifts. More detail about each component of the two-stage bursty/steady model shown in Figure 1 is covered in Section 3.3.

3.2. Sample

We quantified trends in SFH by focusing on the evolution of individual DM halos in Renaissance. Halos grow through a combination of accretion and mergers with other halos, tracked using the halo finder ROCKSTAR (P. S. Behroozi et al. 2013a) and merger trees generated with CONSISTENT TREES (P. S. Behroozi et al. 2013b). The main progenitor halos in these trees represent the most massive progenitor at each step going back in time. We preferentially select halos with smoother merger histories that typically have uncomplicated SFHs. We leave modeling of more violent mergers for future work. Halos that experience large virial mass decreases in their growth histories due to complicated mergers or other factors were excluded from our sample.

To calibrate the semianalytic model, we gathered a sample of 27 DM halo and stellar mass histories illustrative of typical metal-enriched star formation in Renaissance halos. For each halo in our sample, we visually identify when every starburst and quiescent period occurs along with the start of steady star formation. In Figure 2, we show metal-enriched SFHs for seven different halos. A halo typically progresses through a bursty stage with intermittent star formation followed by a steady stage, but can sometimes bypass the bursty stage entirely if star formation begins after the halo exceeds $T_{\text{vir, steady}}$.

3.3. Star Formation Parameterization

Our two-stage metal-enriched star formation model has four key physical quantities. In the bursty stage this includes the mass formed in a starburst M_{burst} and a quiescent period following a burst t_{quies} . The steady stage begins once the virial temperature threshold, T_{vir} , is exceeded, signaling the start of the steady stage. Steady star formation then proceeds at a constant efficiency f_{II} .

We focus our calibration on three different aspects of Pop III formation in Renaissance. The three aspects are when Pop III stars form inside halos, the total Pop III stellar mass produced once formation conditions are met, and how much time must pass after the formation of Pop III before the formation of metal-enriched stars.

Overall, we focus on connecting star formation to halo properties such as the virial mass and do not generally consider environmental properties, with the exception of feedback from

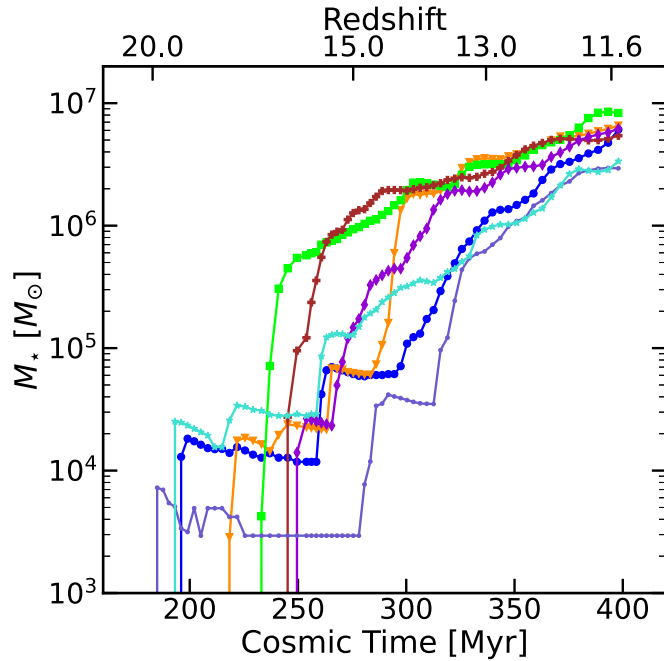


Figure 2. Metal-enriched SFHs for seven Renaissance halos in our sample. Halos can undergo one or multiple bursts and can also skip the bursty stage, instead exhibiting star formation consistent with the steady stage (green and brown).

cosmic reionization. However, as we discuss below in Section 4.2, environmental properties such as the large-scale overdensity or different physics in massive halos could impact star formation. A summary of all model parameters along with best fit values discussed in the following sections can be found in Table 1.

3.3.1. Metal-enriched Star Formation

For the bursty stage, we evaluated multiparameter log scale power-law fits using least squares regression from the SCIPY curve-fit package for the burst masses and quiescent periods in our sample. We also determine standard deviations to account for the distributions of M_{burst} and t_{quies} .

In Figure 3, we find that the metal-enriched burst masses in our sample are closely correlated with both the halo virial mass and the redshift of the burst. We parameterize the stellar mass formed in a burst as

$$M_{\text{burst}} = \alpha \left(\frac{M_{\text{vir}}}{10^7 M_{\odot}} \right)^{\gamma} \left(\frac{1+z}{20} \right)^{\delta} M_{\odot} \quad (1)$$

where M_{vir} and z are, respectively, the halo virial mass and redshift before a starburst. The best fit parameters are $\alpha = 5.364 \times 10^3$, $\gamma = 1.092$, and $\delta = 0.578$. The distribution of the sample around M_{burst} is approximately log-normal with a standard deviation of $\log_{10}(M_{\text{burst}}/M_{\odot}) = 0.408$. As halos reach higher masses at lower redshift, the stellar mass of metal-enriched stars formed in a burst increases.

For the quiescent periods following a starburst, we find a strong negative correlation with the halo virial mass, as shown in Figure 4. The best fit is

$$t_{\text{quies}} = \epsilon \left(\frac{M_{\text{vir}}}{10^7 M_{\odot}} \right)^{\kappa} \text{Myr} \quad (2)$$

where M_{vir} is the virial mass following a starburst and the best fit parameters are $\epsilon = 4.481$ and $\kappa = -0.394$. The distribution of the sample around t_{quies} is approximately log-normal with a standard deviation of $\log_{10}(t_{\text{quies}}/\text{Myr}) = 0.255$. As halos increase in mass, building up deeper gravitational potential wells better able to hold onto gas, a typical quiescent period declines from ~ 100 to ~ 10 Myr for halo masses between $\sim 10^7$ and $10^8 M_{\odot}$.

If shorter quiescent periods are related to the retention of gas reservoirs that fuels subsequent star formation, then the rate the halo is accreting mass should impact the length of the quiescent period. A fast growing halo could potentially recover gas ejected from a starburst and reduce the quiescent period before the next instance of star formation accordingly. We parameterized this effect by considering the time for a halo to double in virial mass following a starburst, t_{double} (see Figure 4). Incorporating t_{double} in our power law did not significantly change the overall fit, with the variance of the sample data from the fit being reduced by less than 20%. Therefore, we do not include t_{double} in the final fits.

With the start of the steady stage, we found that the transition occurs at virial temperatures within a factor of 2 of $T_{\text{vir,steady}} = 1.76 \times 10^4$ K corresponding to an ionization feedback mass for almost all SFHs in our sample. We assume a mean molecular weight of $\mu = 0.6$ consistent with fully ionized primordial gas for the temperature (R. Barkana & A. Loeb 2001). Due to the small range in temperature, we define the onset of the steady stage to occur once the virial temperature exceeds $T_{\text{vir,steady}}$. The virial temperature at the beginning of the steady stage showed weak or no correlation with other halo properties.

Once the steady stage is underway, we found metal-enriched star formation to be well described using a system of differential equations presented in S. R. Furlanetto & J. Mirocha (2022). These coupled equations derive the evolution of both the gas and stellar mass of a halo using a simplified implementation of the “bathtub” model (e.g., N. Bouché et al. 2010; R. Davé et al. 2012; A. Dekel & N. Mandelker 2014):

$$\dot{M}_{*} = \frac{f_{\text{II}}}{t_{\text{ff}}} M_{\text{gas}}, \quad (3)$$

$$\dot{M}_{\text{gas}} = \dot{M}_{\text{acc}} - \dot{M}_{*} - \eta_{\text{SN}} \dot{M}_{*}, \quad (4)$$

where \dot{M}_{*} is the stellar mass growth rate, \dot{M}_{gas} is the rate of change in halo gas mass, \dot{M}_{acc} is the halo gas accretion rate, f_{II} is star formation efficiency, t_{ff} is the freefall time assumed to be a tenth of the Hubble time (which corresponds to the dynamical time at the virial radius of a DM halo described in A. Loeb & S. R. Furlanetto 2013), and η_{SN} is the gas ejection efficiency for SNe feedback.

Two parameters that warrant further discussion are the SNe ejection efficiency, η_{SN} , and steady star formation efficiency, f_{II} . We determine η_{SN} using a similar prescription to F. Sassano et al. (2021), with an SNe ejection efficiency of

$$\eta_{\text{SN}} = \beta \times \frac{2E_{\text{SN}}\epsilon_{\text{SN}}R_{\text{SN}}}{v_{\text{esc}}^2}, \quad (5)$$

where E_{SN} is the average SNe explosion energy, ϵ_{SN} is the SNe kinetic energy conversion fraction, R_{SN} is the SNe rate per mass, v_{esc} is the escape velocity from the halo, and β is the SNe ejection scale factor.

Table 1
Parameters for Star Formation in the Semianalytic Model

Parameter	Description	Fit Values	Standard Deviation
M_{burst}	Metal-enriched starburst mass	$\alpha = 5.364 \times 10^3$ $\gamma = 1.092$ $\delta = 0.578$	0.408
t_{quies}	Quiescent period following metal-enriched starburst	$\epsilon = 4.481$ $\kappa = -0.394$	0.255
f_{II}	Star formation efficiency during steady stage	0.013	0.422
$M_{\text{Total,PopIII}}$	Total Pop III stellar mass formed after halo exceeds M_{\min}	$150 M_{\odot}$	0.371
t_{delay}	Delay before metal-enriched star formation	0.01–100 Myr	...

Note. M_{burst} is given by Equation (1). t_{quies} is given by Equation (2). f_{II} is given by the best fit metal-enriched star formation efficiencies in Figure 5. $M_{\text{Total,PopIII}}$ is described in Section 3.3.2. M_{burst} , t_{quies} , f_{II} , and $M_{\text{Total,PopIII}}$ each follow a log-normal distribution. The last column shows the standard deviation of the \log_{10} of the corresponding quantity as mentioned in the text. t_{delay} is described in Section 3.3.2 and follows a log-uniform distribution.

We assume the average energy for E_{SN} is 10^{51} erg (K. Nomoto et al. 2006). With most of the energy from an SNe lost as thermal energy, only a small fraction is converted into kinetic energy coupled to the gas (S. Walch & T. Naab 2015). We adopt a value of $\epsilon_{\text{SN}} = 1.6 \times 10^{-3}$ for this efficiency that is calibrated to observations (F. Sassano et al. 2021). For R_{SN} , we use metal-enriched SNe feedback energy per mass in agreement with Renaissance of 6.8×10^{48} erg M_{\odot}^{-1} (J. H. Wise et al. 2012b). Dividing this quantity by E_{SN} yields an SNe rate of $R_{\text{SN}} = 6.8 \times 10^{-3} M_{\odot}^{-1}$. Finally, v_{esc} is set to be the circular velocity of a halo excluding a factor of $\sqrt{2}$ in the numerator of the escape velocity using the relation $\sqrt{GM/r_{\text{vir}}}$ from R. Barkana & A. Loeb (2001).

We lower the SNe efficiency using an SNe ejection scale factor β calibrated to high-mass halos. Values between $\beta = 0$ and 0.1 generate star formation consistent with our sample and we find $\beta = 0.01$ produces total metal-enriched star formation that agrees well with Renaissance. For $\beta = 1.0$, η_{SN} significantly suppresses star formation in the most massive halos, producing stellar masses around an order of magnitude lower than Renaissance due to the efficient ejection of a large fraction of gas early in the steady stage.

To calibrate the steady star formation efficiency in Equation (3) to Renaissance, we determine values for f_{II} in agreement with our sample of metal-enriched SFHs using the following method. First, we separate the steady stage from the bursty stage for each SFH in our sample. We set the initial stellar mass equal to Renaissance and assume the gas mass is consistent with the cosmic baryon fraction of the halo virial mass. Next, we evolve Equations (3) and (4) over the entire steady stage and perform a regression using the SCIPY curve-fit package to determine the best fit for f_{II} .

Figure 5 shows the distribution of best fit steady stage star formation efficiencies. We find the distribution is roughly log-normal and centered around a mean efficiency of $f_{\text{II}} = 0.013$ with a standard deviation of $\log_{10}(f_{\text{II}}) = 0.422$. The predicted metal-enriched stellar mass using the best fit efficiency with Equations (3) and (4) at most deviates from Renaissance by a factor of ~ 1.5 . We note that outliers such as the low efficiency of $f_{\text{II}} = 0.0006$ have a large impact on the variance of the distribution due to the small sample size.

We found that a halo mass dependent f_{II} of the functional form $f_{\text{II}} M_{\text{vir}}^{\tau}$ also produced good fits for the Renaissance SFHs

of most halos during the steady stage. However, for the largest halos at low redshift, this produces unphysically high star formation efficiencies, and therefore we do not include it in our model.

3.3.2. Pop III Star Formation

Pop III stars form in pristine metal-free halos that exceed the minimum mass where dense gas clouds can condense due to cooling from roto-vibrational molecular hydrogen transitions (Z. Haiman et al. 1996a, 1996b; M. Tegmark et al. 1997; M. E. Machacek et al. 2001). The H₂ fraction is fundamental to determine if a halo forms Pop III stars and is included as a formation condition in Renaissance accordingly (see Section 2). Therefore, physical processes that change the H₂ fraction are important to consider.

Lyman-Werner photons with energies between 11.2 and 13.6 eV emitted by the first stars can efficiently photodissociate H₂ through the two-step Solomon process (T. P. Stecher & D. A. Williams 1967). The LW photons travel over cosmological scales to neighboring metal-free halos, suppressing H₂ cooling and the formation of Pop III stars (A. Dekel & M. J. Rees 1987; Z. Haiman et al. 1997, 2000; M. E. Machacek et al. 2001; J. H. Wise & T. Abel 2007; B. W. O’Shea & M. L. Norman 2008; K. Ahn et al. 2009; E. Visbal et al. 2014). We follow A. Fialkov et al. (2013) to compute the minimum mass for molecular cooling that can form stars in minihalos using the relation,

$$M_{\text{H}_2} = 2.5 \times 10^5 \left(\frac{1+z}{26} \right)^{-3/2} \times [1 + 6.96(4\pi J_{\text{LW},21})^{0.47}] M_{\odot} \quad (6)$$

where the first term is the minimum halo mass in the absence of an LW background to suppress H₂ determined using the same assumptions as E. Visbal et al. (2020) and $J_{\text{LW},21}$ is the local LW background in units of 10^{-21} erg s⁻¹ cm⁻² Hz⁻¹ sr⁻¹. We use the background presented in H. Xu et al. (2016) that self-consistently calculates an LW background from star formation in the Normal region.

Once a halo reaches virial temperatures of $T_{\text{vir,steady}} \gtrsim 10^4$ K, collisionally excited line emission from atomic hydrogen becomes the dominant cooling process. For the atomic cooling

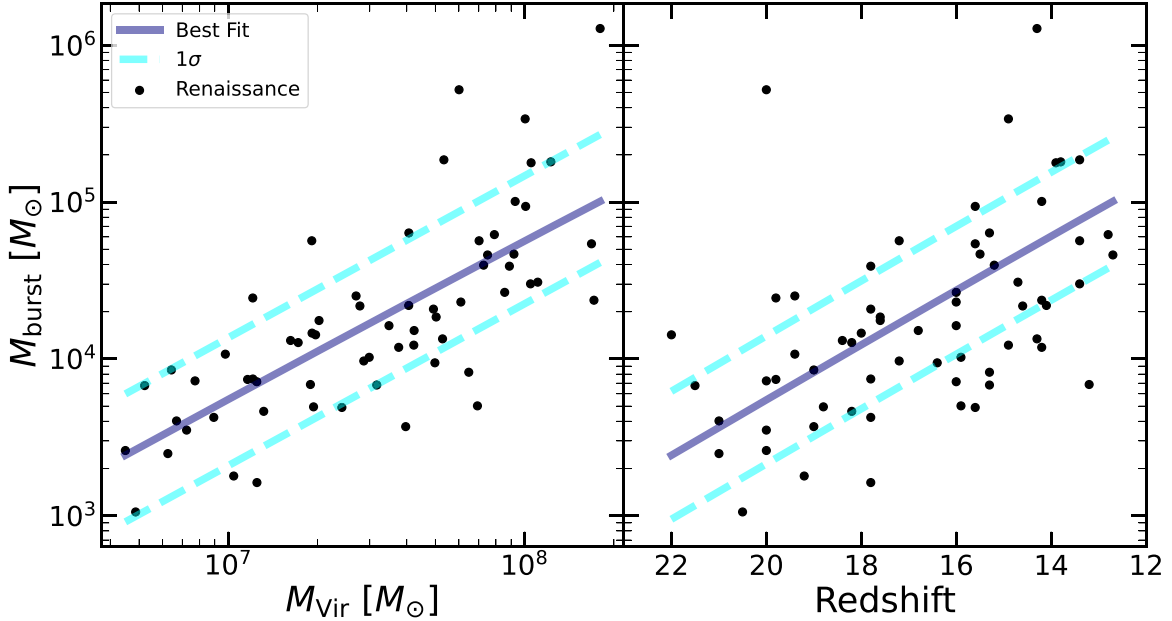


Figure 3. Metal-enriched starburst masses from the sample of Renaissance halos during the bursty stage. Best fit two parameter power law (solid-blue lines) along with 1σ lines (dashed-cyan lines). Burst mass increases for larger mass halos and at lower redshifts.

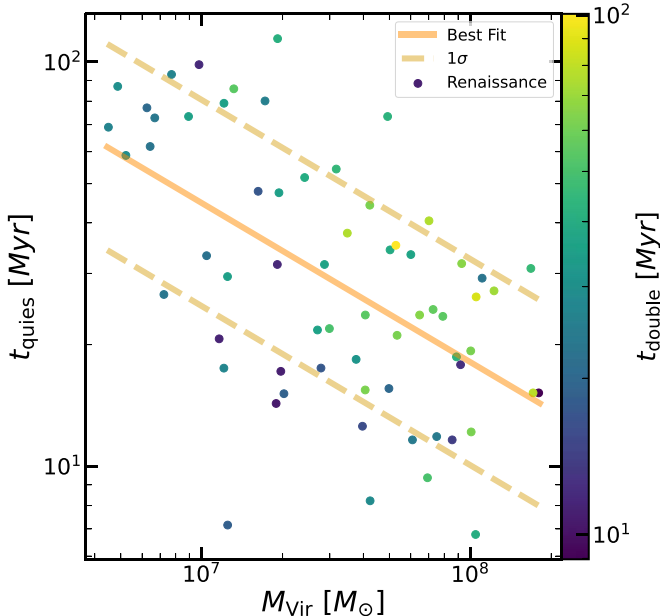


Figure 4. Quiescent times from the sample of Renaissance halos during the bursty stage. Power-law best fit (solid-orange line) and 1σ lines (dashed-gold lines). The color bar values correspond to the time in millions of years it takes the halo to double in virial mass. Overall, the quiescent time between star formation events decreases for higher mass halos.

mass threshold we adopt the relation,

$$M_a = 5.4 \times 10^7 \left(\frac{1+z}{11} \right)^{-3/2} M_\odot \quad (7)$$

which is determined using the cosmological hydrodynamical simulations of R. Fernandez et al. (2014).

The Renaissance simulations have a DM mass resolution of $2.9 \times 10^4 M_\odot$ and the halo mass function is well resolved for halos with masses $\gtrsim 2 \times 10^6 M_\odot$ (B. W. O’Shea et al. 2015). This artificially sets a lower-limit on the minimum halo mass scale for Pop III star formation. Simulations by M. Kulkarni

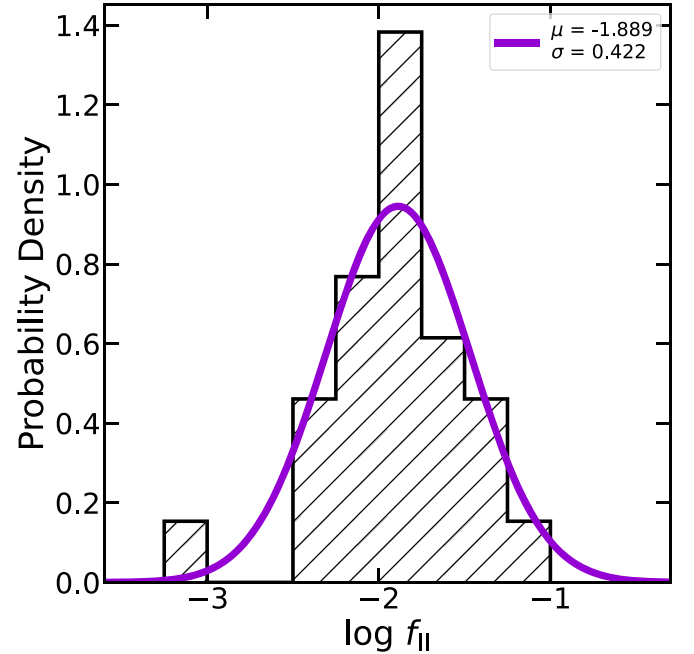


Figure 5. Metal-enriched star formation efficiencies for the steady stage in Renaissance halos. Each f_{II} were determined by finding the best fit for Equations (3) and (4) during the steady stage of a halo in the sample.

et al. (2021) and A. T. P. Schauer et al. (2021) find minimum masses of order 10^5 – $10^6 M_\odot$ at high redshift for similar LW backgrounds which are unable to be resolved by Renaissance. Therefore, we adopt a mass resolution limit of $4 \times 10^6 M_\odot$ below which Pop III is assumed to be unable to form. This allows our model to closely reproduce Pop III star formation by delaying star formation in unresolved low-mass halos similarly to Renaissance.

Our primary goal was to empirically match the amount of Pop III star formation in Renaissance with the semianalytic model. If we instead impose a minimum halo mass for Pop III

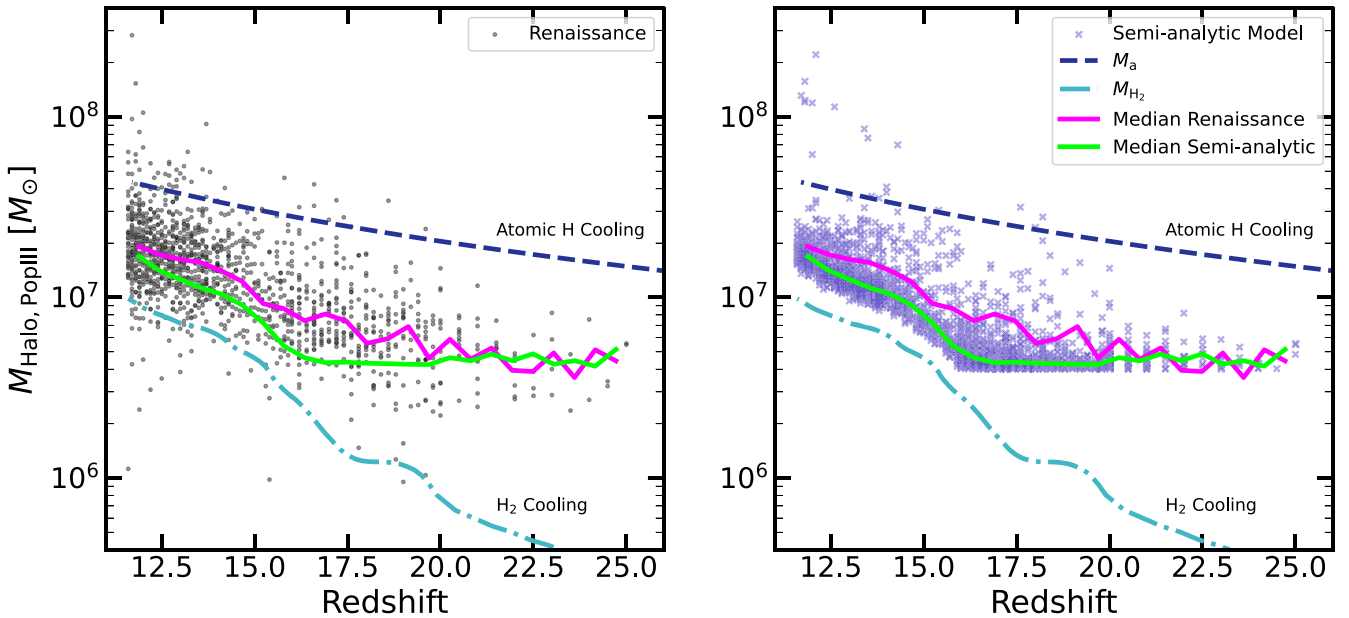


Figure 6. DM masses of halos that host the first Pop III star formation for Renaissance (left-hand panel) and one realization of the semianalytic model (right-hand panel). We show the median halo mass hosting Pop III for Renaissance (magenta line) and the semianalytic model (green line). The dashed and dotted-dashed curves show M_a and M_{H_2} , respectively. The sharp cut-off in halo mass for the semianalytic model in the right-hand panel is due to the mass resolution limit of $4 \times 10^6 M_\odot$.

star formation of $2 \times 10^6 M_\odot$, our model produces many more Pop III stars than Renaissance. This is due to a discrepancy where in the simulations there is a scatter in the minimum halo mass for Pop III star formation (as a result of the numerical resolution), while in our model it is a constant halo mass threshold. Scatter in the critical halo mass for star formation increases the abundance of Pop III stars.

The left-hand panel of Figure 6 shows the DM halo masses of Renaissance halos that host the first Pop III star formation, $M_{\text{Halo,PopIII}}$, as a function of redshift. We include M_a and M_{H_2} using a $J_{\text{LW},21}$ equivalent to the global LW background (a larger local value for $J_{\text{LW},21}$ than the background would result in a higher M_{H_2}).

To produce Pop III stellar masses consistent with Renaissance, we determined the total mass of Pop III stars formed during the initial instance of star formation in Renaissance halos. We found that the total Pop III mass, $M_{\text{Total,PopIII}}$, closely follows a log-normal distribution centered on a mass of $\approx 150 M_\odot$ with a standard deviation of $\log_{10}(M_{\text{Total,PopIII}}/M_\odot) = 0.371$. Both the virial mass of the halo and the redshift were found to have minimal correlation with total Pop III mass formed.

Finally, we calculated the typical delay between the first Pop III SNe in a halo, occurring after a mass-dependent stellar lifetime from D. Schaerer (2002), with the beginning of metal-enriched star formation. Figure 7 shows the distribution of the delay times as a function of halo mass. We find three distinct populations of delay times. One population has metal-enriched star formation starting rapidly between 0.01 and 0.1 Myr after the first Pop III supernova. Another population has delays between 0.1 and 3 Myr and a final smaller group has longer delay times of 10–100 Myr. We investigated deeper potential wells in high-mass halos retaining metal-enriched gas, ionizing feedback suppressing star formation, and powerful Pop III SNe as physical origins for these three populations. However, the delay times show little to no correlation with halo mass, virial temperature, and total SNe energy emitted by Pop III stars before the onset of metal-enriched formation.

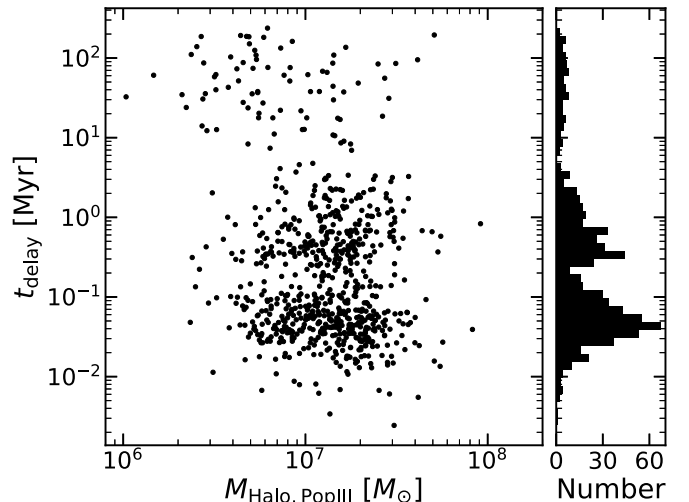


Figure 7. The delay period before the formation of metal-enriched stars following the death of the first Pop III star compared with the dark mass halo mass at formation of Pop III.

The halos that begin to form metal-enriched stars after less than a million years are of particular interest due to the short timescales for metals to be dispersed into the nearby ISM. In this case, star formation is triggered in nearby clumps that have survived the radiative phase of the Pop III stars. An SN blastwave will compress the clumps above the density threshold for star formation; however, some of these cases could be artificial. It is possible that a number of these clumps may meet the criteria for star formation in the simulation but are not gravitationally bound and should instead dissipate sometime later. The typical Renaissance output cadence of ~ 4 Myr hinders further investigation into these clumps and the underlying cause of the quick transition to metal-enriched star formation. To be as consistent with Renaissance as possible,

we consider a t_{delay} ranging between 0.01 and 100 Myr with the understanding that numerical issues could be responsible for the shortest delays.

4. Model Modifications and Results

We modify the semianalytic model introduced in E. Visbal et al. (2020) which is based on DM halo merger trees from cosmological N -body simulations and incorporates star formation at a constant efficiency, feedback from Lyman–Werner radiation, and growth of H II regions in the intergalactic medium. These processes are calculated on a grid using fast-Fourier transforms (FFTs) using 3D spatial positions and clustering of halos.

Star formation in the updated semianalytic model consists of Pop III formation followed by two stages of metal-enriched star formation with a bursty and steady stage. The calibration to Renaissance is implemented by including a minimum mass for Pop III star formation, M_{\min} , along with total Pop III stellar masses and delay periods before the beginning of metal-enriched star formation that are consistent with Renaissance. Additionally, for metal-enriched star formation we introduce our findings for M_{burst} , t_{quies} , $T_{\text{vir,steady}}$, and f_{II} from the bursty and steady stages previously presented in Section 3.3.1. See Table 1 for a concise overview of the implementation into the model. Finally, we do not include external enrichment in our calibrations. External enrichment of neighboring star-forming halos was found to marginally increase the metal-enriched SFRD and slightly reduce the Pop III SFRD in E. Visbal et al. (2020). While this does not preclude external enrichment being more important in dense, highly clustered environments, for now we leave calibration to external enrichment in Renaissance for future work.

Now, we will cover the modifications to the E. Visbal et al. (2020) model in more detail. We assume the minimum mass for Pop III star formation to be the minimum of M_{H_2} and M_a with a mass resolution lower-limit of $\gtrsim 4 \times 10^6 M_{\odot}$ from Section 3.3.2. For the local LW background $J_{\text{LW},21}$ term in M_{H_2} , an external background is included in addition to the local component from Pop III and metal-enriched stellar mass. We implement a background that self-consistently calculates an LW background from star formation in the Normal region discussed in Section 3.3.2. If a halo with no prior star formation is located in an ionized region, we increase the minimum mass to $M_{\min} = 1.5 \times 10^8 \left(\frac{1+z}{11}\right)^{-3/2} M_{\odot}$ (in agreement with M. Dijkstra et al. 2004).

The right-hand panel of Figure 6 shows $M_{\text{Halo,PopIII}}$ predicted by our model. There are two differences between our model and Renaissance that are important to highlight. First, values of $M_{\text{Halo,PopIII}}$ in our model are much more tightly clustered at lower halo masses than Renaissance. A potential consequence of this behavior is that the same halo in our model sometimes can form Pop III at a lower halo mass corresponding to an earlier time. Second, $M_{\text{Halo,PopIII}}$ in Renaissance is typically smaller for $z > 17$ and higher for $z < 17$ compared to the semianalytic model. Additionally, $M_{\text{Halo,PopIII}}$ displays greater variability for Renaissance. The consequences of these differences will be further discussed in Section 4.2.

Once the mass of a halo exceeds M_{\min} , we use the findings for Pop III formation discussed in Section 3.3.2. First, we randomly sample a total Pop III stellar mass from the log-normal Renaissance distribution centered on $\approx 150 M_{\odot}$. Then,

we assign a delay period before metal-enriched star formation can begin, t_{delay} , that ranges between 0.01 and 100 Myr. Note that we also tested using a probability distribution function set to exactly match the histogram in the right-hand panel of Figure 7 and our results were essentially unchanged.

After t_{delay} following Pop III star formation has elapsed, we determine if a halo is the bursty or steady stage by comparing its virial temperature to the $T_{\text{vir,steady}} = 1.76 \times 10^4 \text{ K}$ threshold. If in the bursty stage, we determine the total stellar mass formed in a starburst by randomly sampling from a log-normal distribution centered on M_{burst} from Equation (1). A quiescent period sampled from another log-normal distribution centered on t_{quies} from Equation (2) is assigned to the halo and its descendants. The halo will then either experience a subsequent starburst after the quiescent period has passed or it will exceed the $T_{\text{vir,steady}}$ threshold and enter the steady star formation stage.

At the beginning of the steady stage, we initially assume the halo contains gas consistent with the cosmic baryon fraction of its virial mass. A star formation efficiency, f_{II} , is then randomly sampled from the roughly log-normal distribution in Figure 5. This efficiency will be passed to all descendants of this halo unless a merger with other halos in the steady stage occurs. Then, the average of progenitor halo star formation efficiencies is assigned to the descendant instead. We calculate metal-enriched star formation and follow the subsequent evolution of gas mass using Equations (3) and (4), respectively.

4.1. Individual Star Formation Histories

To determine the effectiveness of our calibration, we compare different realizations of our model with Renaissance for metal-enriched halo SFHs. We begin by running 10 different random seeds of our semianalytic model on the Renaissance DM halo merger trees. Figure 8 shows a selection of metal-enriched SFHs from our simulations. The top left-hand panel shows the metal-enriched SFH for the most massive halo in the Renaissance Normal region. The large second starburst and high $f_{\text{II}} \approx 0.1$ are extreme values in our distributions for M_{burst} and f_{II} , making them correspondingly difficult to reproduce in our model. The SFHs in the top right-hand and bottom right-hand panels transition from the bursty to the steady stage differently from Renaissance. Our fixed threshold for the transition at $T_{\text{vir,steady}} = 1.76 \times 10^4 \text{ K}$ can lead to more starbursts or an earlier transition to the steady stage, by the final simulation redshift, the total star formation produced during the steady stage lies within the scatter produced by the model. The bottom left-hand panel shows a SFH with bursty and steady stages that fall well within the scatter of our model.

Generally, there is good agreement between SFHs produced by the semianalytic model and Renaissance. By the final simulation redshift when metal-enriched stars dominate, star formation for Renaissance halos typically lie within the range predicted by our model and agreement for the best model is within a factor of 2. Additionally, the chaotic bursty stage is also well reproduced if metal-enriched star formation begins at a similar time.

While the overall agreement with Renaissance is considerable, the model does not perfectly capture the variance in individual SFHs. Our choice to calibrate to a sample of main progenitor halos without violent major mergers in Renaissance could potentially not be fully representative of all halos. Additionally, the differential equations used during the steady

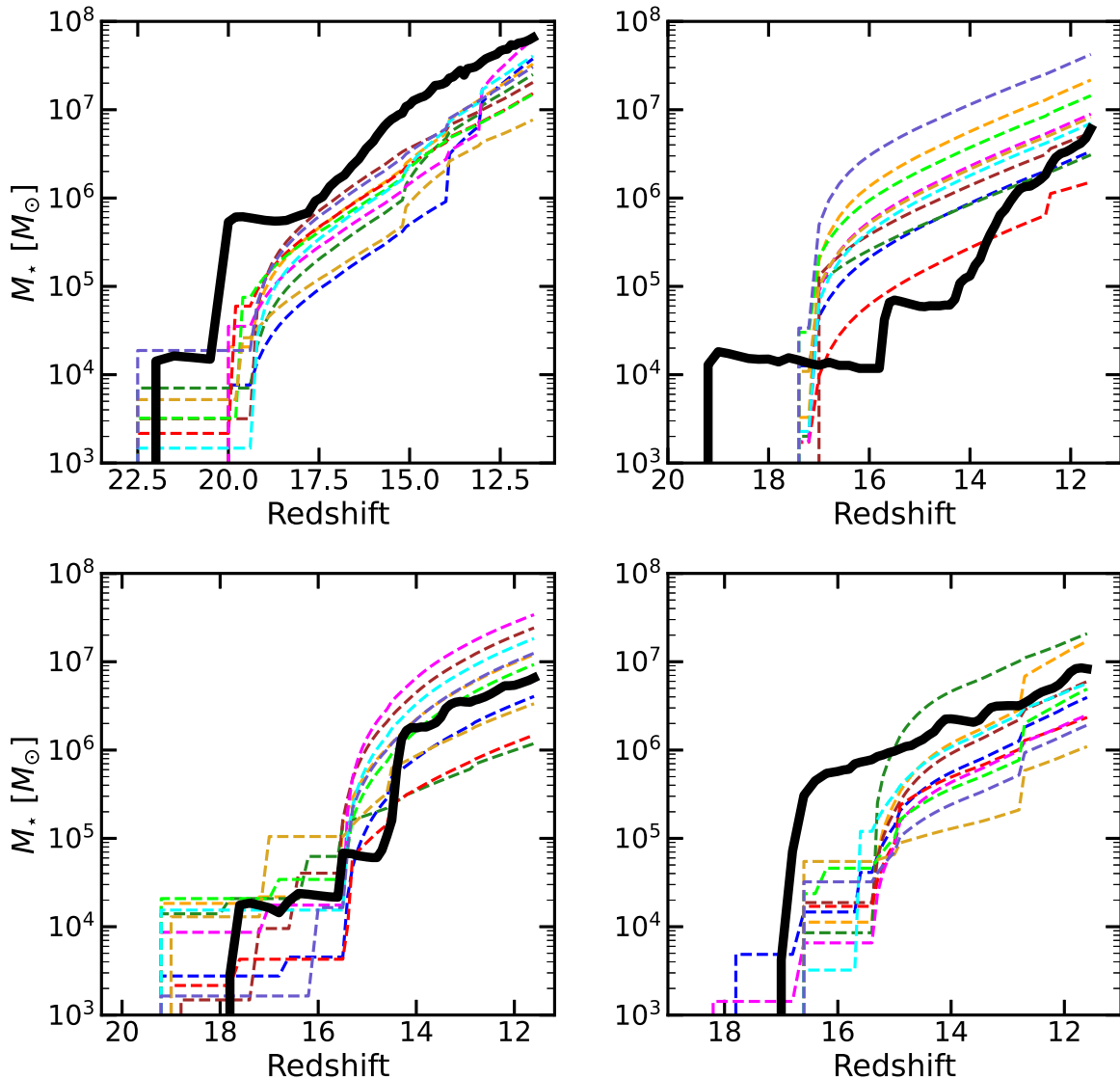


Figure 8. Total metal-enriched stellar masses and redshifts of four different main progenitor halos. The Renaissance metal-enriched SFH (black line) is compared with 10 different realizations of the semianalytic model (dashed lines).

stage produce star formation that is smoother than Renaissance, lacking variations in star formation that often occur. Regardless, the simplified prescription for metal-enriched star formation is often able to reproduce SFHs in the mass range of 10^6 – $10^8 M_\odot$ remarkably well.

4.2. Total Star Formation Rate

Extending from the individual SFHs discussed in the previous section, we also compare SFRDs averaged throughout the simulation box to evaluate how well 10 different realizations of our model reproduce star formation across entire Renaissance volumes.

First, we will focus on metal-enriched star formation shown in the top row of Figure 9. In the top left-hand panel of Figure 9, we find that our model produces a metal-enriched SFRD consistent with the Renaissance Normal region within a factor of ~ 2 . The good agreement with the Renaissance SFRD indicates that our two-stage metal-enriched star formation model, when aggregated for many halo SFHs, is able to closely reproduce total star formation in a large volume.

In addition to our simulations using the calibrations to the Normal region, we also consider the Void and RarePeak regions not included in our sample of halos (mentioned in Section 2). To ensure consistency with Renaissance, we introduce a different LW background produced by Pop III stars used in J. H. Wise et al. (2012b) for the RarePeak region. For the Void region, we use the same LW background as the Normal region (see Section 3.3.2).

Results for the Void region are shown in the middle column of Figure 9. The metal-enriched SFRD of the model is typically within a factor of ~ 2 of Renaissance and at most differs by a factor of ~ 3 . For $z < 16$, the steady stage begins in an increasing number of halos and will begin to dominate the metal-enriched SFRD. The scatter in the metal-enriched SFRD produced by our model begins to narrow as a consequence of the smooth SFHs produced during the steady stage mentioned in Section 4.1. This results in an SFRD that exhibits much less variation than Renaissance and could explain the difference with the semianalytic model at $z < 16$.

In the right-hand column of Figure 9, we show our model results for the RarePeak region. Metal-enriched star formation

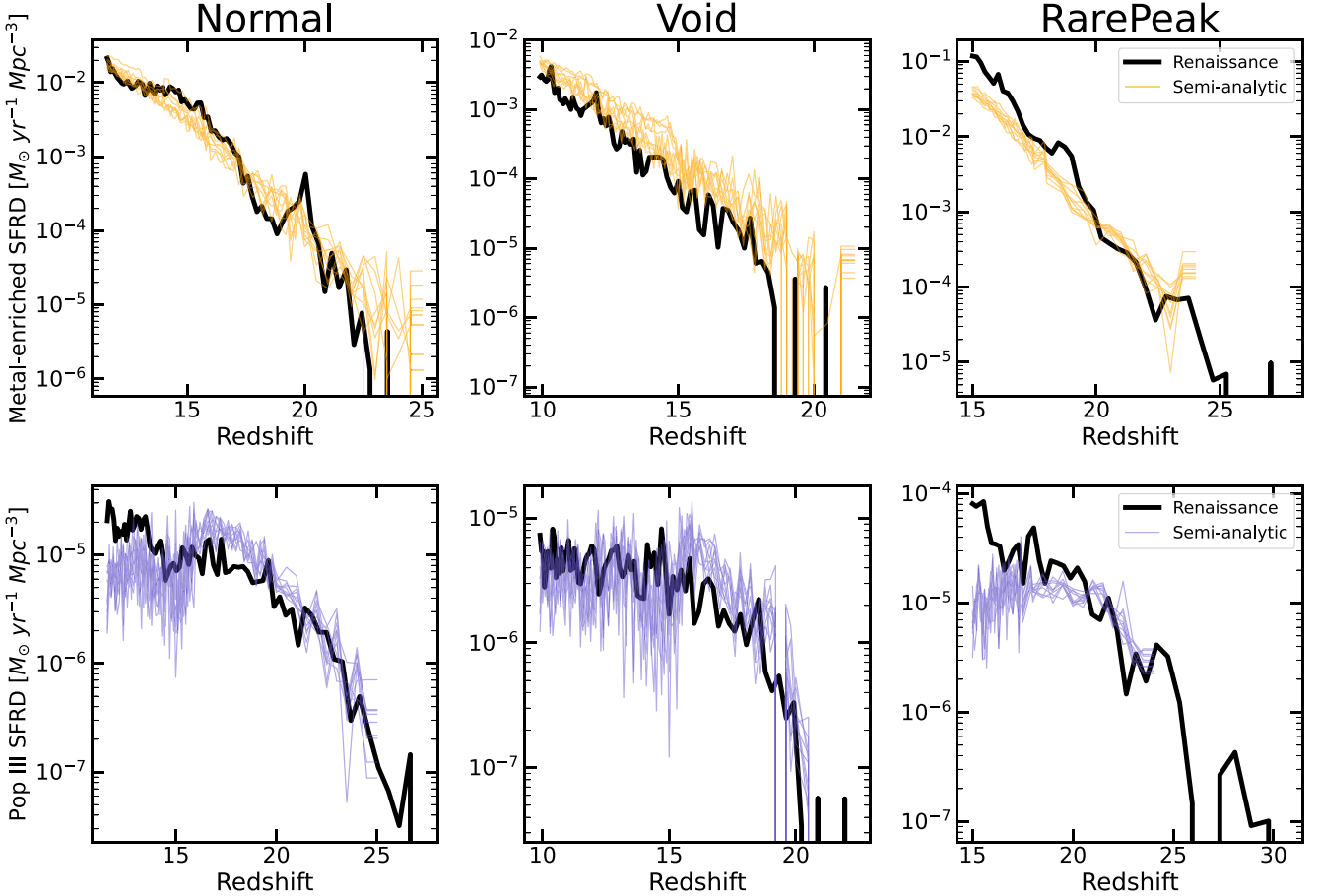


Figure 9. Cosmic SFRDs for both metal-enriched (orange lines, top row) Pop III (blue lines, bottom row) compared to Renaissance (black lines). Results for the Normal, Void, and RarePeak volumes are shown in the left-hand, middle, and right-hand columns, respectively. Overall, our model produces metal-enriched SFRDs typically within a factor of ~ 2 of Renaissance for a variety of environments. The larger discrepancy found at lower redshift in Void and RarePeak will be investigated in future work.

in Renaissance agrees within a factor of ~ 2 for $z > 19$ but eventually is more efficient than our model by a factor of ~ 3 by $z \sim 15$. The source of this discrepancy is currently unknown, but we speculate that a potential explanation is that some physics are missing from our prescription. For example, it has been shown that accretion driven mergers can boost star formation by increasing torques and driving gas toward the center of a halo (P. F. Hopkins et al. 2013). This could explain the discrepancies we find in both Void and RarePeak.

Next, we will discuss Pop III star formation. Again, it is important to note that Renaissance has difficulties in resolving halos with masses $\lesssim 4 \times 10^6 M_\odot$. Therefore, we focused mainly on calibration without going into the same level of detail as we do for metal-enriched star formation. As shown in the bottom row of Figure 9, the Pop III SFRDs produced by the semianalytic model for Normal, Void, and RarePeak demonstrate similar behavior. The Pop III SFRD first increases, and then rests at the same value before gradually decreasing. This is due to small discrepancies in the M_{\min} prescription in the semianalytic model compared to Renaissance.

We considered adding halos from the Void and RarePeak regions to increase the size of the sample. To combine the halos from each region to produce a global SFRD, the dependence of the SFRD on the mean density must be considered. Determining this functional dependence is beyond the scope of this work. However, matter density fluctuations in the Universe are roughly linear at high redshift. Linearity implies that the

distribution of overdensity averaged over volumes such as Normal, Void, or RarePeak is peaked at zero. Therefore, we know that volumes such as the Normal region would contribute significantly to the global SFRD. Additionally, we have identified that environmental effects impact star formation in these regions. Until we better understand the physics involved, we chose to only calibrate based on the Normal sample such that our model describes typical densities in the Universe.

We conclude that our model is able to reproduce the Renaissance SFRDs within a factor of ~ 2 for the Normal region. For the Void and RarePeak regions not used during the calibration of our model, the agreement is similar to the Normal at high- z and varies at low- z to a factor of ~ 2 and ~ 3 for Void and RarePeak, respectively. In future work, incorporating additional physics dependent on environmental effects could improve the agreement between our model and Renaissance.

4.3. Comparison with Updated Prescription for Pop III Stars

Another question that may be interesting to consider is the impact of incorporating recent findings updating the minimum halo mass of Pop III star formation, M_{\min} , with new physics. In M. Kulkarni et al. (2021), M_{\min} is obtained as a function of LW background (including H₂ self-shielding), redshift, and baryon-DM streaming. While we were able to calibrate to the Renaissance Pop III SFRD within a factor of ~ 2 , it is

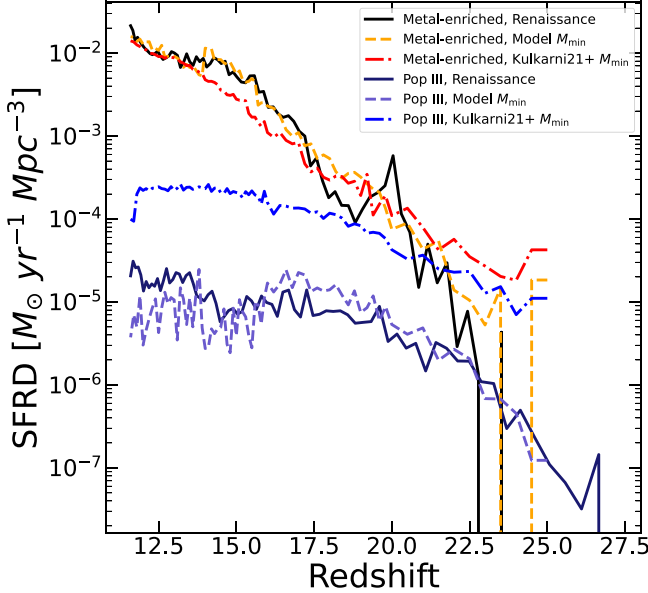


Figure 10. Cosmic metal-enriched and Pop III SFRDs compared with Renaissance for different M_{\min} prescriptions in our model. The M_{\min} with the mass resolution limit used in this paper (dashed lines) produces a Pop III SFRD that is roughly an order of magnitude lower than the Pop III SFRD using M_{\min} from M. Kulkarni et al. (2021). The metal-enriched SFRDs agree within a factor of ~ 2 except for $z > 18$.

important to emphasize again that Renaissance is limited in resolving minihalos that form Pop III.

When updating our prescription for M_{\min} to be consistent with M. Kulkarni et al. (2021) and removing the mass resolution limit, we find in Figure 10 a Pop III SFRD approximately an order of magnitude higher than the prescription calibrated to Renaissance. This is due to the inclusion of H₂ self-shielding, which lowers the impact of $J_{\text{LW},21}$ on M_{\min} . The impact on metal-enriched star formation due to the increased amount of Pop III was marginal. The metal-enriched SFRD from our semianalytic prescription both with and without the updated M_{\min} along Renaissance agree within a factor of ~ 2 for $z < 18$. This result can be heavily influenced by any changes to LW feedback and reionization, along with localized metal enrichment of halos not included in our model. Determining the relative impact of these processes after further calibration to Renaissance will be the goal of future work. Our method will allow this work to be done with minimal computational expense and is a key benefit of semianalytic models.

4.4. H II Regions

To determine the size and growth of ionized H II regions, we apply the same FFT method as E. Visbal et al. (2020). Using a 256^3 cubic grid, we find the total number density of ionizing photons produced by DM halos that have escaped in the surrounding IGM in each cell. This is calculated as $P_{\text{cell}} = f_{\text{esc,II}} \eta_{\text{II}} M_{*,\text{II,cell}} / (m_{\text{proton}} V_{\text{cell}}) + f_{\text{esc,III}} \eta_{\text{III}} M_{*,\text{III,cell}} / (m_{\text{proton}} V_{\text{cell}})$, where $f_{\text{esc,II}}$ and $f_{\text{esc,III}}$ are the escape fractions of hydrogen ionizing photons from halos in a cell containing metal-enriched and Pop III stars. The number of hydrogen ionizing photons produced per baryon for metal-enriched and Pop III stars is assumed to be $\eta_{\text{II}} = 4000$ and $\eta_{\text{III}} = 65,000$, respectively. The metal-enriched value corresponds to a Salpeter IMF from 0.1 to $100 M_{\odot}$ and metallicity $Z = 0.0004$

(see Table 1 in S. Samui et al. 2007). Note, if values were used for η that correspond directly with Renaissance, we would expect f_{esc} to change accordingly but the overall ionization fraction and structure would remain the same. The Pop III value is expected to be emitted from a $\sim 40 M_{\odot}$ star over its lifetime (D. Schaefer 2002). Both $M_{*,\text{II,cell}}$ and $M_{*,\text{III,cell}}$ are the total stellar masses ever formed by halos in a cell. Finally, V_{cell} is the comoving volume of a single cell. For each cell, P_{cell} is then smoothed over a range of spherical bubble sizes and is selected as the center of an H II bubble if it exceeds a threshold of $i_{\text{thres}} = 4\bar{n}_{\text{H}}$ (E. Visbal et al. 2020).

The extent of ionized H II regions determines when halos first form stars through the minimum halo mass for Pop III star formation and if a halo's descendants ever form metal-enriched stars in our model with no external enrichment. The top panel of Figure 11 compares the total ionization fraction in our model to Renaissance. We calibrated the escape fraction of ionizing radiation to $f_{\text{esc,II}} = 0.02$ for metal-enriched stars and $f_{\text{esc,III}} = 0.1$ for Pop III stars to produce a total fraction of the IGM ionized by our model within a factor of 2 of Renaissance by $z \sim 11$.

In the middle and bottom panels of Figure 11, we compare ionized bubble sizes in our model and Renaissance for halos in the same thin volume at $z = 11.6$. The difference in the H II regions produced by our model in this region demonstrates the limitations of our current approach in reproducing ionization in simulations such as Renaissance. We find that our model typically produces larger ionized bubbles than Renaissance. These H II regions extend from massive halos with substantial star formation and are generally found at the center of clustered environments. To address this discrepancy, we are currently improving the prescription to produce more realistic bubbles and this will be the focus of future work (T. Behling et al. 2025, in preparation).

5. Summary and Discussion

In this paper we explored the calibration of a semianalytic model to the Renaissance Simulations, radiative hydrodynamical simulations of the first stars and galaxies. An accurate semianalytic model can make computationally efficient predictions in a fraction of the time, finishing in less than a day on a laptop compared to the ~ 10 million core hours on the Blue Waters supercomputer used for a single Renaissance simulation. The efficiency of semianalytic models allows them to complement other simulations by extending over larger volumes, reaching lower redshifts, and exploring parameter space (e.g., Pop III IMF). While this work is focused on the Renaissance Simulations, the same methodology can be straightforwardly implemented in other semianalytic calculations and may be readily applied to other simulations.

To construct a semianalytic model consistent with Renaissance, we assembled a sample of SFHs and calibrate our model to them. For metal-enriched star formation, we introduced a two-stage model (that does not include external enrichment) consisting of an early bursty formation stage that transitions to a steady stage with star-forming at a constant efficiency. Notably, we implemented stochastic elements during star formation not typically included in other models by sampling parameters from the distributions in Table 1. We find that our stochastic two-stage model typically produced metal-enriched SFHs consistent with Renaissance, but completely capturing

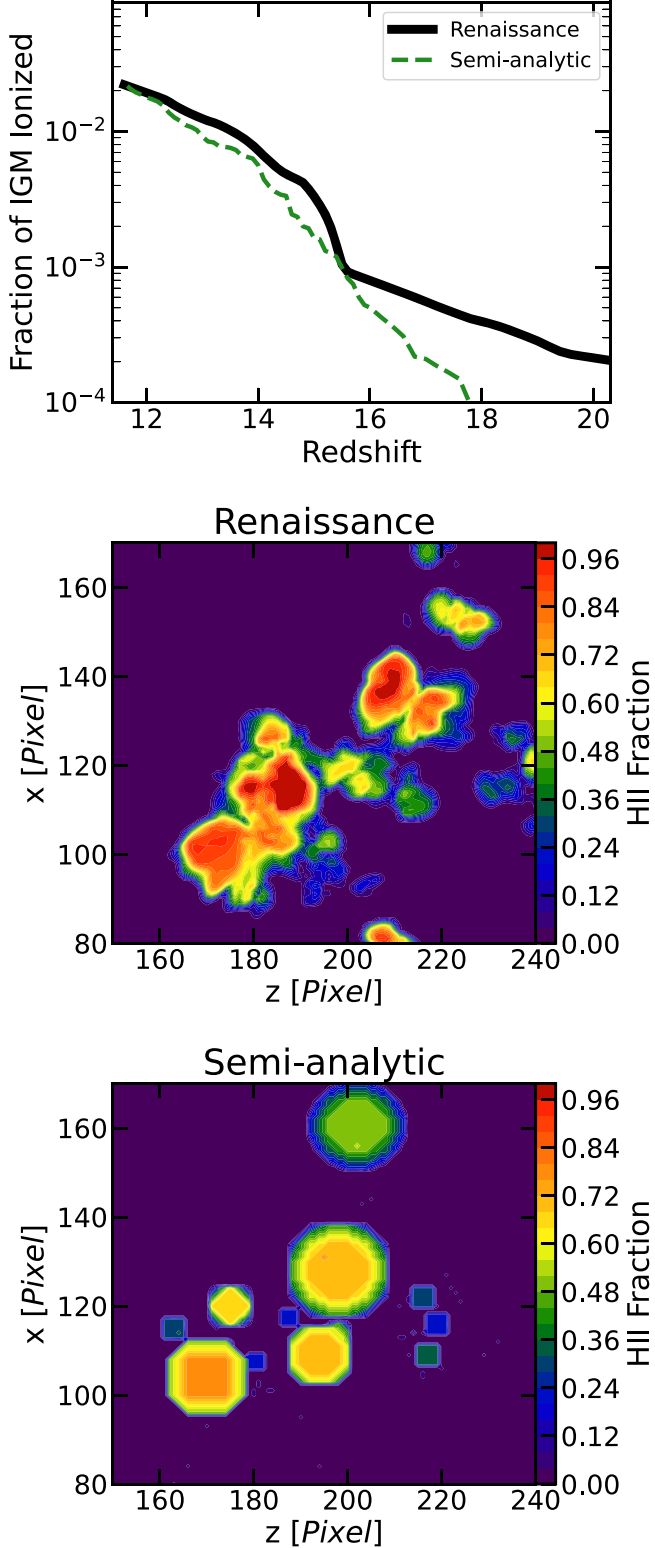


Figure 11. Top panel: mean fraction of the volume of the IGM that is ionized in Renaissance (black line) compared with the semianalytic model (green-dashed line). Projections of the H II fraction for a region with a width and depth of ≈ 2.7 and ≈ 0.33 comoving Mpc, respectively. Middle panel: Renaissance. Bottom panel: semianalytic model.

the variance in individual SFHs was not the intent of our model.

To calibrate Pop III star formation, we implemented a minimum halo mass consistent with when the first stars form in

Renaissance. Once halos exceed this mass, a total Pop III stellar mass was assigned to halos along with a delay period before the onset of metal-enriched star formation. These values are sampled from the distributions described in Table 1. Our approach can be used to easily calibrate to different Pop III prescriptions and incorporate them into the model.

We determined how closely our model is able to reproduce the Renaissance cosmic SFH by comparing evolution of SFRDs and found agreement within a factor of ~ 2 for redshifts $11 < z < 25$ for halo masses $\lesssim 10^9 M_\odot$. We also tested our model on both the rarefied Void and overdense RarePeak regions in Renaissance. The metal-enriched SFRDs produced by our model typically agrees by a factor of ~ 2 in Void and ~ 3 in RarePeak, respectively. The difference in SFRDs based on environment suggests that there are physics not currently included in our model that either lead to higher star formation efficiencies or increased external enrichment. Therefore, we expect that semianalytic models that do not consider these effects will fail to reproduce star formation by similar factors.

Additionally, while reproducing the Renaissance star formation was a primary goal, our Pop III prescription could be updated to include more recent findings. For example, it has been shown that baryon-DM streaming, self-shielding from LW radiation, and X-ray feedback impact the H₂ fraction, and therefore halo minimum mass for Pop III formation. A combination of these effects can raise the minimum halo mass and delay the formation of the first stars. We found using the minimum DM halo mass for Pop III formation from M. Kulkarni et al. (2021) that the Pop III SFRD increases by about an order of magnitude compared to Renaissance. Meanwhile, for $z < 20$ the metal-enriched SFRDs agree within a factor of ~ 2 . Both LW feedback and metal enrichment could impact star formation and will be the focus of future work implementing additional calibrations to Renaissance.

Using the grid-based approach of E. Visbal et al. (2020) to calculate feedback from LW radiation using FFTs, we found that our model produces total ionized fractions that agree within a factor of ~ 2 to Renaissance between redshifts $16 \lesssim z \lesssim 11$. When comparing individual H II regions, we found that our model typically forms larger ionized bubbles than those in Renaissance. H II regions in highly clustered environments can suppress the onset of star formation in neighboring halos and could reduce the overall amount of metal-enriched and Pop III stars.

In our future work, we plan to investigate the impact of the environment on star formation in greater detail. Including dependence on large-scale overdensity, external enrichment, and a more detailed treatment of ionized H II bubble formation in our calibration could potentially improve the agreement with Renaissance for different environments. Our two-stage prescription for metal-enriched star formation would then be more accurate for a range of cosmological environments.

We also intend to make observational predictions by applying our calibrated model to DM merger trees that extend over a large statistically representative volume. Some of these predictions include SNe rates (e.g., E. Scannapieco et al. 2005; S. M. Weinmann & S. J. Lilly 2005; J. H. Wise & T. Abel 2005; A. Mesinger et al. 2006; J. A. Hummel et al. 2012; T. Pan et al. 2012; J. L. Johnson et al. 2013; M. Tanaka et al. 2013; D. J. Whalen et al. 2013b; R. S. de Souza et al. 2014; T. Hartwig et al. 2018), luminosity functions (e.g., R. J. Bouwens et al. 2023; H. Atek et al. 2024), and abundance

predictions in strong gravitational lenses. Incorporating direct collapse black hole seeds in our model and tracking their growth could also potentially lead to new insights into the supermassive black holes found at the centers of most galaxies.

Acknowledgments

We thank Greg Bryan and Zoltan Haiman for useful discussions. R.H. and E.V. acknowledge support from NASA ATP grant 80NNSSC22K0629 and NSF grant AST-2009309. J.W. acknowledges support by NSF grant AST-2108020 and NASA grants 80NSSC20K0520 and 80NSSC21K1053. The numerical simulations in this paper were run on the Ohio Supercomputer Center (OSC).

Software: NUMPY (C. R. Harris et al. 2020), SCIPY (P. Virtanen et al. 2020), MATPLOTLIB (J. D. Hunter 2007), CYTHON (S. Behnel et al. 2011), JUPYTER NOTEBOOK (T. Kluyver et al. 2016), ROCKSTAR (P. S. Behroozi et al. 2013a), CONSISTENT TREES (P. S. Behroozi et al. 2013b), YT (M. J. Turk et al. 2011), YTREE (B. Smith & M. Lang 2019).

ORCID iDs

Ryan Hazlett  <https://orcid.org/0000-0002-1034-7986>
 Mihir Kulkarni  <https://orcid.org/0000-0002-9789-6653>
 Eli Visbal  <https://orcid.org/0000-0002-8365-0337>
 John H. Wise  <https://orcid.org/0000-0003-1173-8847>

References

- Abe, M., Yajima, H., Khochfar, S., Dalla Vecchia, C., & Omukai, K. 2021, *MNRAS*, 508, 3226
- Abel, T., Anninos, P., Zhang, Y., & Norman, M. L. 1997, *NewA*, 2, 181
- Abel, T., Bryan, G. L., & Norman, M. L. 2002, *Sci*, 295, 93
- Ahn, K., Shapiro, P. R., Iliev, I. T., Mellema, G., & Pen, U.-L. 2009, *ApJ*, 695, 1430
- Arrabal Haro, P., Dickinson, M., Finkelstein, S. L., et al. 2023, *Natur*, 622, 707
- Atek, H., Labb  , I., Furtak, L. J., et al. 2024, *Natur*, 626, 975
- Barkana, R., & Loeb, A. 2001, *PhR*, 349, 125
- Behnel, S., Bradshaw, R., Citro, C., et al. 2011, *CSE*, 13, 31
- Behroozi, P. S., Wechsler, R. H., & Wu, H.-Y. 2013a, *ApJ*, 762, 109
- Behroozi, P. S., Wechsler, R. H., Wu, H.-Y., et al. 2013b, *ApJ*, 763, 18
- Borrow, J., Kannan, R., Garaldi, E., et al. 2023, *MNRAS*, 525, 5932
- Bouch  , N., Dekel, A., Genzel, R., et al. 2010, *ApJ*, 718, 1001
- Bouwens, R. J., Stefanon, M., Brammer, G., et al. 2023, *MNRAS*, 523, 1036
- Bowman, J. D., Rogers, A. E. E., Monsalve, R. A., Mozdzen, T. J., & Mahesh, N. 2018, *Natur*, 555, 67
- Brummel-Smith, C., Bryan, G., Butsky, I., et al. 2019, *JOSS*, 4, 1636
- Bryan, G. L., Norman, M. L., O’Shea, B. W., et al. 2014, *ApJS*, 211, 19
- Bunker, A. J., Saxena, A., Cameron, A. J., et al. 2023, *A&A*, 677, A88
- Chen, P., Wise, J. H., Norman, M. L., Xu, H., & O’Shea, B. W. 2014, *ApJ*, 795, 144
- Cohen, A., Fialkov, A., Barkana, R., & Lotem, M. 2017, *MNRAS*, 472, 1915
- Crosby, B. D., O’Shea, B. W., Smith, B. D., Turk, M. J., & Hahn, O. 2013, *ApJ*, 773, 108
- Dav  , R., Finlator, K., & Oppenheimer, B. D. 2012, *MNRAS*, 421, 98
- de Souza, R. S., Ishida, E. E. O., Whalen, D. J., Johnson, J. L., & Ferrara, A. 2014, *MNRAS*, 442, 1640
- Dekel, A., & Mandelker, N. 2014, *MNRAS*, 444, 2071
- Dekel, A., & Rees, M. J. 1987, *Natur*, 326, 455
- Dijkstra, M., Haiman, Z., Rees, M. J., & Weinberg, D. H. 2004, *ApJ*, 601, 666
- Eisenstein, D. J., Willott, C., Alberts, S., et al. 2023, arXiv:2306.02465
- Fernandez, R., Bryan, G. L., Haiman, Z., & Li, M. 2014, *MNRAS*, 439, 3798
- Fialkov, A., Barkana, R., Visbal, E., Tseliakhovich, D., & Hirata, C. M. 2013, *MNRAS*, 432, 2909
- Finkelstein, S. L., Bagley, M. B., Ferguson, H. C., et al. 2023, *ApJL*, 946, L13
- Frebel, A., & Norris, J. E. 2015, *ARA&A*, 53, 631
- Furlanetto, S. R., & Mirocha, J. 2022, *MNRAS*, 511, 3895
- Gao, L., & Theuns, T. 2007, *Sci*, 317, 1527
- Gnedin, N. Y. 2000, *ApJ*, 542, 535
- Gnedin, N. Y., & Hui, L. 1998, *MNRAS*, 296, 44
- Greif, T. H. 2015, *ComAC*, 2, 3
- Greif, T. H., Springel, V., White, S. D. M., et al. 2011, *ApJ*, 737, 75
- Haiman, Z., Abel, T., & Rees, M. J. 2000, *ApJ*, 534, 11
- Haiman, Z., Rees, M. J., & Loeb, A. 1996a, *ApJ*, 467, 522
- Haiman, Z., Rees, M. J., & Loeb, A. 1997, *ApJ*, 476, 458
- Haiman, Z., Thoul, A. A., & Loeb, A. 1996b, *ApJ*, 464, 523
- Harris, C. R., Millman, K. J., van der Walt, S. J., et al. 2020, *Natur*, 585, 357
- Hartwig, T., Bromm, V., & Loeb, A. 2018, *MNRAS*, 479, 2202
- Hegde, S., & Furlanetto, S. R. 2023, *MNRAS*, 525, 428
- Heger, A., Fryer, C. L., Woosley, S. E., Langer, N., & Hartmann, D. H. 2003, *ApJ*, 591, 288
- Hirano, S., Hosokawa, T., Yoshida, N., et al. 2014, *ApJ*, 781, 60
- Hoeft, M., Yepes, G., Gottl  ber, S., & Springel, V. 2006, *MNRAS*, 371, 401
- Hopkins, P. F., Cox, T. J., Hernquist, L., et al. 2013, *MNRAS*, 430, 1901
- Hosokawa, T., Omukai, K., Yoshida, N., & Yorke, H. W. 2011, *Sci*, 334, 1250
- Hummel, J. A., Pawlik, A. H., Milosavljevi  , M., & Bromm, V. 2012, *ApJ*, 755, 72
- Hunter, J. D. 2007, *CSE*, 9, 90
- Ishigaki, M. N., Tominaga, N., Kobayashi, C., & Nomoto, K. 2018, *ApJ*, 857, 46
- Johnson, J. L., Dalla, V. C., & Khochfar, S. 2013, *MNRAS*, 428, 1857
- Kluyver, T., Ragan-Kelley, B., P  rez, F., et al. 2016, in Positioning and Power in Academic Publishing: Players, Agents and Agendas, ed. F. Loizides & B. Schmidt (Amsterdam: IOS Press), 87
- Komatsu, E., Smith, K. M., Dunkley, J., et al. 2011, *ApJS*, 192, 18
- Kulkarni, M., Visbal, E., & Bryan, G. L. 2021, *ApJ*, 917, 40
- Kulkarni, M., Visbal, E., Bryan, G. L., & Li, X. 2022, *ApJL*, 941, L18
- Liu, B., & Bromm, V. 2020, *MNRAS*, 497, 2839
- Loeb, A., & Furlanetto, S. R. 2013, The First Galaxies in the Universe (Princeton, NJ: Princeton Univ. Press)
- Machacek, M. E., Bryan, G. L., & Abel, T. 2001, *ApJ*, 548, 509
- Maiolino, R., Uebler, H., Perna, M., et al. 2024, *A&A*, 687, A67
- McCaffrey, J., Hardin, S., Wise, J., & Regan, J. 2023, *OJAp*, 6, 47
- Mebane, R. H., Mirocha, J., & Furlanetto, S. R. 2018, *MNRAS*, 479, 4544
- Mesinger, A., Johnson, B. D., & Haiman, Z. 2006, *ApJ*, 637, 80
- Mocz, P., Fialkov, A., Vogelsberger, M., et al. 2019, *PhRvL*, 123, 141301
- Mocz, P., Fialkov, A., Vogelsberger, M., et al. 2020, *MNRAS*, 494, 2027
- Nebrin, O., Giri, S. K., & Mellema, G. 2023, *MNRAS*, 524, 2290
- Noh, Y., & McQuinn, M. 2014, *MNRAS*, 444, 503
- Nomoto, K., Tominaga, N., Umeda, H., Kobayashi, C., & Maeda, K. 2006, *NuPhA*, 777, 424
- Okamoto, T., Gao, L., & Theuns, T. 2008, *MNRAS*, 390, 920
- O’Shea, B. W., & Norman, M. L. 2007, *ApJ*, 654, 66
- O’Shea, B. W., & Norman, M. L. 2008, *ApJ*, 673, 14
- O’Shea, B. W., Wise, J. H., Xu, H., & Norman, M. L. 2015, *ApJL*, 807, L12
- Pan, T., Kasen, D., & Loeb, A. 2012, *MNRAS*, 422, 2701
- Parsons, J., Mas-Ribas, L., Sun, G., et al. 2022, *ApJ*, 933, 141
- Riaz, S., Hartwig, T., & Latif, M. A. 2022, *ApJL*, 937, L6
- Samui, S., Srianand, R., & Subramanian, K. 2007, *MNRAS*, 377, 285
- Sassano, F., Schneider, R., Valiante, R., et al. 2021, *MNRAS*, 506, 613
- Scannapieco, E., Madau, P., Woosley, S., Heger, A., & Ferrara, A. 2005, *ApJ*, 633, 1031
- Schaerer, D. 2002, *A&A*, 382, 28
- Schauer, A. T. P., Glover, S. C. O., Klessen, R. S., & Clark, P. 2021, *MNRAS*, 507, 1775
- Shapiro, P. R., Giroux, M. L., & Babul, A. 1994, *ApJ*, 427, 25
- Smith, B., & Lang, M. 2019, *JOSS*, 4, 1881
- Smith, B. D., Turk, M. J., Sigurdsson, S., O’Shea, B. W., & Norman, M. L. 2009, *ApJ*, 691, 441
- Sobacchi, E., & Mesinger, A. 2013, *MNRAS*, 432, L51
- Stecher, T. P., & Williams, D. A. 1967, *ApJL*, 149, L29
- Susa, H., Hasegawa, K., & Tominaga, N. 2014, *ApJ*, 792, 32
- Tanaka, M., Moriya, T. J., & Yoshida, N. 2013, *MNRAS*, 435, 2483
- Tegmark, M., Silk, J., Rees, M. J., et al. 1997, *ApJ*, 474, 1
- Thoul, A. A., & Weinberg, D. H. 1996, *ApJ*, 465, 608
- Trenti, M., & Stiavelli, M. 2009, *ApJ*, 694, 879
- Turk, M. J., Smith, B. D., Oishi, J. S., et al. 2011, *ApJS*, 192, 9
- Virtanen, P., Gommers, R., Oliphant, T. E., et al. 2020, *NatMe*, 17, 261
- Visbal, E., Barkana, R., Fialkov, A., Tseliakhovich, D., & Hirata, C. M. 2012, *Natur*, 487, 70
- Visbal, E., Bryan, G. L., & Haiman, Z. 2020, *ApJ*, 897, 95
- Visbal, E., Haiman, Z., & Bryan, G. L. 2015, *MNRAS*, 450, 2506
- Visbal, E., Haiman, Z., & Bryan, G. L. 2018, *MNRAS*, 475, 5246
- Visbal, E., Haiman, Z., Terrazas, B., Bryan, G. L., & Barkana, R. 2014, *MNRAS*, 445, 107
- Walch, S., & Naab, T. 2015, *MNRAS*, 451, 2757
- Wang, X., Cheng, C., Ge, J., et al. 2024, *ApJL*, 967, L42

- Weinmann, S. M., & Lilly, S. J. 2005, *ApJ*, **624**, 526
Whalen, D. J., Even, W., Frey, L. H., et al. 2013b, *ApJ*, **777**, 110
Whalen, D. J., Fryer, C. L., Holz, D. E., et al. 2013a, *ApJL*, **762**, L6
Wise, J. H., & Abel, T. 2005, *ApJ*, **629**, 615
Wise, J. H., & Abel, T. 2007, *ApJ*, **671**, 1559
Wise, J. H., & Abel, T. 2011, *MNRAS*, **414**, 3458
Wise, J. H., Abel, T., Turk, M. J., Norman, M. L., & Smith, B. D. 2012a, *MNRAS*, **427**, 311
Wise, J. H., Turk, M. J., Norman, M. L., & Abel, T. 2012b, *ApJ*, **745**, 50
Xu, H., Ahn, K., Wise, J. H., Norman, M. L., & O’Shea, B. W. 2014, *ApJ*, **791**, 110
Xu, H., Wise, J. H., Norman, M. L., Ahn, K., & O’Shea, B. W. 2016, *ApJ*, **833**, 84
Yoshida, N., Abel, T., Hernquist, L., & Sugiyama, N. 2003, *ApJ*, **592**, 645
Yung, L. Y. A., Somerville, R. S., Finkelstein, S. L., Popping, G., & Davé, R. 2019, *MNRAS*, **483**, 2983